Journal of Materials Chemistry A

PAPER

View Article Online
View Journal | View Issue

Cite this: J. Mater. Chem. A, 2019, 7, 23868

Selectivity for ethanol partial oxidation: the unique chemistry of single-atom alloy catalysts on Au, Ag, and Cu(111)†

Hao Li,* Wenrui Chai and Graeme Henkelman*

Received 2nd May 2019
Accepted 15th May 2019

DOI: 10.1039/c9ta04572d

rsc.li/materials-a

Recently, we found that the atomic ensemble effect is the dominant effect influencing catalysis on surfaces alloyed with strong- and weak-binding elements, determining the activity and selectivity of many reactions on the alloy surface. In this study we design single-atom alloys that possess unique dehydrogenation selectivity towards ethanol (EtOH) partial oxidation, using knowledge of the alloying effects from density functional theory calculations. We found that doping of a strong-binding single-atom element (*e.g.*, Ir, Pd, Pt, and Rh) into weak-binding inert close-packed substrates (*e.g.*, Au, Ag, and Cu) leads to a highly active and selective initial dehydrogenation at the α-C–H site of adsorbed EtOH. We show that many of these stable single-atom alloy surfaces not only have tunable hydrogen binding, which allows for facile hydrogen desorption, but are also resistant to carbon coking. More importantly, we show that a rational design of the ensemble geometry can tune the selectivity of a catalytic reaction.

1. Introduction

Ethanol (EtOH) is an industrially important molecule which is widely used;[1] it is a renewable and sustainable energy carrier, featuring easy production, transportation, and storage.[2,3] Many chemical processes and applications involve the activation of EtOH on catalytic materials, including hydrogen production, fuel cells, steam reforming, and the production of high value products through EtOH oxidation and/or cross-coupling.[4–10] In the past decade, both experimental and theoretical research have been reported regarding EtOH (partial) oxidation with thermal- and electro-catalytic methods which can be used in fuel cells and other applications.[11–15] Interestingly, many of the studies have shown that EtOH is not always completely oxidized and thus, the initial dehydrogenation is the most important step that largely determines the subsequent reaction pathways and the final oxidation products.[12,15–21] Therefore, the competing initial scission of the O–H, α-C–H, and β-C–H bonds has been studied with the idea that knowledge of this chemistry can lead to significant advances in catalytic materials design.[11,12,15,22–27] In many experimental studies on transition metal close-packed surfaces, it was found that the initial H-abstraction is one of the rate-determining steps for EtOH decomposition, with subsequent steps occurring rapidly.[15,22–26] Also, it was found that reactions between oxygen/hydroxyl and the EtOH species involving the α-carbon are more facile than the initial dehydrogenation of EtOH in aerobic oxidation.[15] Although there could be other rate-determining steps, depending on the specific catalytic surface (including bond cleavage and desorption of intermediate species), the initial dehydrogenation step is one of the most difficult steps for EtOH oxidation, so that the chemistry of this initial dehydrogenation needs to be understood.

Many previous studies have discussed that an understanding of the initial dehydrogenation step of alcohol can help with the design of selective alcohol oxidation and cross-coupling reactions towards higher value products.[7,15,18,28–34] Therefore, the chemistry of this step at a rationally designed surface will provide significant insights into the reaction selectivity. Specifically, the selectivity of scission of the O–H, α-C–H, and β-C–H bonds should provide general guidance for the selective oxidation of different types of alcohols. Notably, our recent combined theoretical and experimental study shows that the initial dehydrogenation of EtOH is the rate-determining and the most important step for determining the selectivity of EtOH partial oxidation towards the formation of ethyl acetate.[15] For EtOH steam reforming, it was found that the initial dehydrogenation of EtOH largely determines the reaction pathway.[8] This also provides insight into the reverse reaction of EtOH synthesis from syngas.[35] However, while previous studies have shown favorable initial dehydrogenation at O–H or β-C–H,[8,19,24,25,36,37] few studies have shown α-C–H selectivity on close-packed surfaces, which dramatically limits the range of possible products for EtOH oxidation.

In our recent studies, bimetallic alloy surfaces were found to possess excellent activity and selectivity for many

Department of Chemistry, The Oden Institute for Computational Engineering and Sciences, The University of Texas at Austin, 105 E. 24th Street, Stop A5300, Austin, Texas 78712, USA. E-mail: lihao@utexas.edu; henkelman@utexas.edu

† Electronic supplementary information (ESI) available. See DOI: 10.1039/c9ta04572d

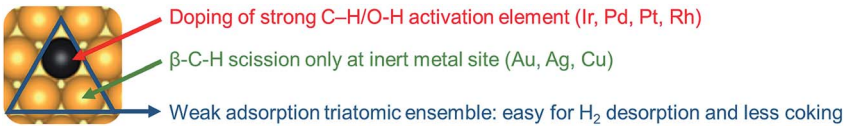

Scheme 1 Ensemble including a strong-binding element doped into an inert substrate. Black and gold spheres represent the single-atom element and the inert element of the substrate, respectively.

industrially important reactions, including hydrogenation[38–40] and dehydrogenation.[26,27,41] It was found that as compared to ligand (electronic)[42] and strain[43] effects, the atomic ensemble effect – the specific arrangement of surface atoms – is the most important for determining the function of a catalyst with an alloy surface.[44] The ensemble effect is important because adsorbate binding is predominantly determined by the local adsorption environment, which can consist of different types of elements at a binding site. Our calculations show that reactions at an alloy surface are site-specific: a surface ensemble pattern could possess high activity and/or unique selectivity that determines the trend of the overall reaction. For dehydrogenation reactions including EtOH partial oxidation, it was found that there are two main factors that influence the catalytic reactivity:[27,45] (i) strong binding of EtOH, or the dehydrogenated-EtOH species, leads to low dehydrogenation barriers and (ii) the surface alloy pattern strongly influences dehydrogenation selectivity. These conclusions are consistent with experiments showing that for EtOH activation on PdAu, higher Pd surface coverage leads to increased bond cleavage and various selective pathways.[26,41] Similar conclusions were reached in studies of formic acid dehydrogenation on PdAu catalysts.[46] Inspired by these experiments, we aim to tailor the alloy pattern and provide a predictive guide for controlling the selectivity of the final products for multistep reactions including EtOH dehydrogenation.

Based upon the alloying effects discussed above, we have developed a strategy for tailoring the ensemble geometry to activate EtOH α-C–H selectivity. Combined with previous results that β-C–H activation can be a favorable initial step on strong-binding elements but less favorable on weak-binding surfaces including Au, Ag, and Cu(111),[27] we can minimize the influence of these strong binding sites by only having one active atom doped on an inert surface (Scheme 1). That is to say, with the most favorable EtOH adsorption geometry where the O–H group points towards a strong binding element,[26,27,41,47] β-C–H activation is only likely to occur at the inert sites of Au, Ag, or Cu, with high energy barriers. In contrast, activation of O–H and α-C–H is facile at the active dopant site. In recent years, some research groups, including the Sykes group, have shown that the synthesis and characterization of similar single-atom alloy single-crystal surfaces including Pd_1/Cu,[48,49] Pt_1/Cu,[50] and Pd_1/Au[51] are possible with state-of-the-art techniques. Specifically, it was found that there are a series of unique features of single-atom alloys that could lead to facile dehydrogenation reactions of relatively small molecules such as methane, ammonia, and methanol.[52] However, the competing activation of hydrogen at different functional groups for more complicated molecules (*e.g.*, EtOH) is not yet comprehensively understood. There are also other important studies that have elucidated the efficient activities of catalysts with doped isolated strong-binding elements,[53–55] indicating that single-atom materials are promising catalysts with industrial importance.

Another feature of these single-atom alloys, which has been shown in many previous studies, is that inert elements including Au, Ag, and Cu are facile for hydrogen desorption and resistant to carbon-coking.[41,56] This is because some alloy bimetallics (*e.g.*, PdAu[38,44]) are highly tunable for hydrogen and carbon binding, having weaker adsorbate bindings at the alloy ensembles compared to strong-binding monometallic surfaces.[26,41] From Scheme 1 we can see that the geometry of a triatomic alloy ensemble (the smallest repeat unit for adsorption in close-packed surfaces,[44] as shown by the blue triangle in Scheme 1) is X_1Y_2 (where X and Y are the strong- and weak-binding elements). The adsorption environment provided by this 3-fold hollow site can possess similar facile hydrogen desorption and coke-resistant properties.

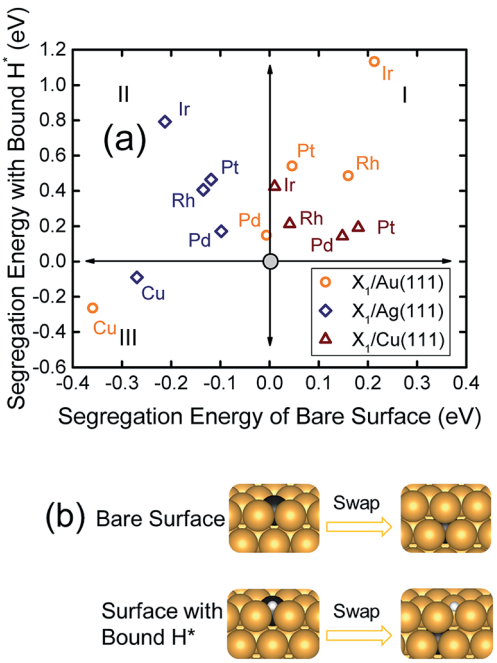

Fig. 1 (a) Stability of the single-atom alloy surfaces. X represents the doped single-atom element (Cu, Ir, Pd, Pt, and Rh). (b) Process by which a sublayer element swaps with the surface dopant. Black, gold, and white spheres represent the single-atom element, the inert substrate element, and hydrogen, respectively.

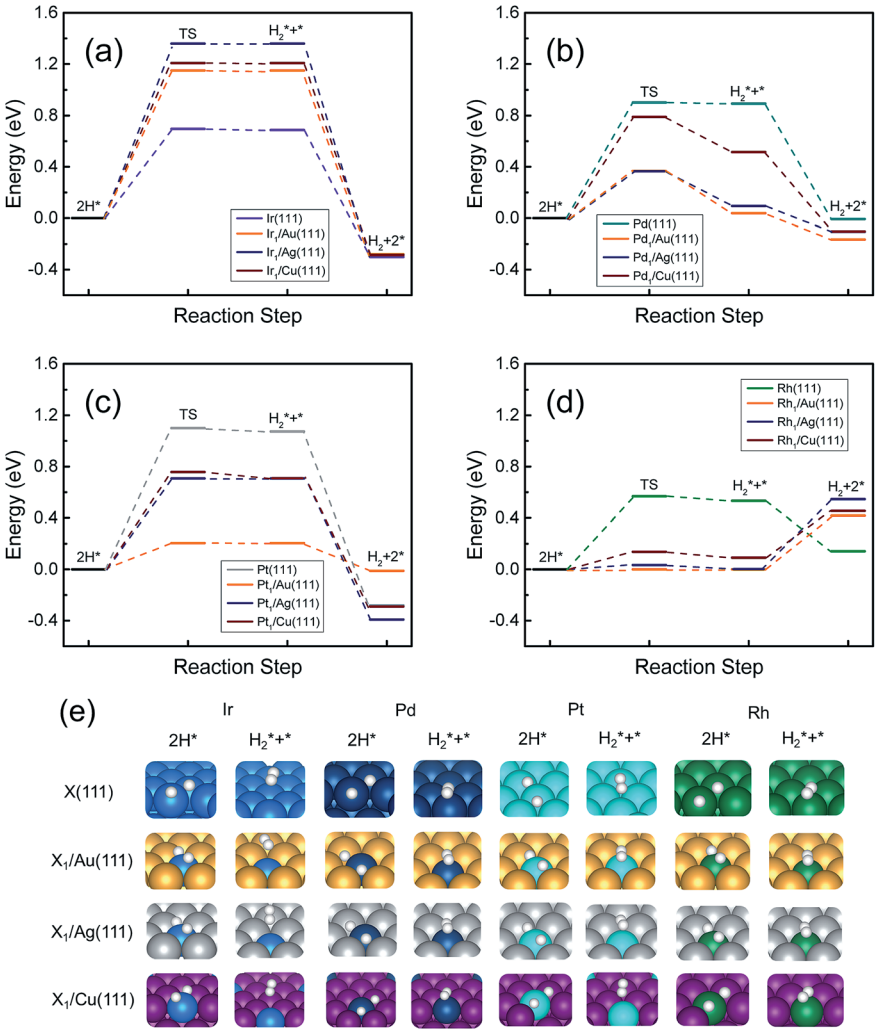

Fig. 2 Reaction pathway of H_2 association and desorption on (a) Ir-, (b) Pd-, (c) Pt-, and (d) Rh-surfaces. Entropy corrections for H_2 were added with a temperature of 298 K. (e) Initial and final states of hydrogen association on the surfaces. Gold, purple, sliver, blue, deep blue, teal, green, and white spheres represent Au, Cu, Ag, Ir, Pd, Pt, Rh, and H, respectively.

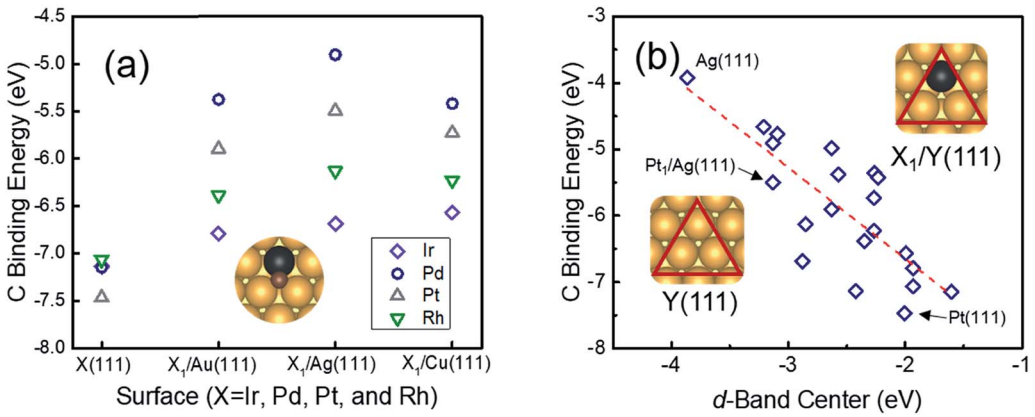

Fig. 3 (a) Calculated carbon binding energies on the single-atom alloy surfaces and their monometallic counterparts. The inset shows the binding configuration of carbon at an alloyed triatomic ensemble. (b) Correlation between the carbon binding energies and the calculated d-band centers of the triatomic ensembles. Insets show the triatomic ensembles that are considered for the calculations of the d-band center. Black, golden, and brown spheres represent X (X = Ir, Pd, Pt, and Rh), Y (Y = Au, Ag, and Cu), and C, respectively.

In this study, we show how theoretical design of a surface ensemble pattern can target an unusual selectivity in EtOH dehydrogenation. Specifically, based upon the fact that the initial dehydrogenation is a crucial step for the selectivity of the final products for ethanol oxidation,[15,17,18,32,57] cross-coupling esterification,[7,15,33] and steam reforming,[8] we focus on the initial dehydrogenation. We show that though α-C–H selectivity is a rarely observed pathway in EtOH dehydrogenation, we are able to find twelve single-atom alloy surfaces that are active and highly selective for α-C–H scission, compared to the competing pathways.

2. Methods

2.1 Computational methods

All the first-principle computations were performed using the VASP code. The generalized gradient approximation method with the Perdew–Burke–Ernzerhof functional (GGA-PBE) was applied to describe the electronic exchange and correlation.[58] Core electrons were described within the projector augmented-wave (PAW) framework.[59] Kohn–Sham wave functions were expanded in a plane wave basis[60] with a kinetic energy cutoff of 400 eV. The van der Waals correction method of Grimme *et al.* (DFT-D3) was included in all the calculations.[47,61] Geometries were considered converged after the forces on each atom fell below 0.05 eV $Å^{-1}$. A $(3 \times 3 \times 1)$ Monkhorst–Pack *k*-point mesh was used to sample the Brillouin zone.[62] The climbing image nudged elastic band (ClNEB) method was used to acquire the activation energy and the transition state geometries,[63] with at least six intermediate images between the initial and final states. Spin polarization was tested and only found to have negligible influence on the results and was therefore not included in most of our calculations. Convergence tests were performed with stricter calculation criteria in our previous

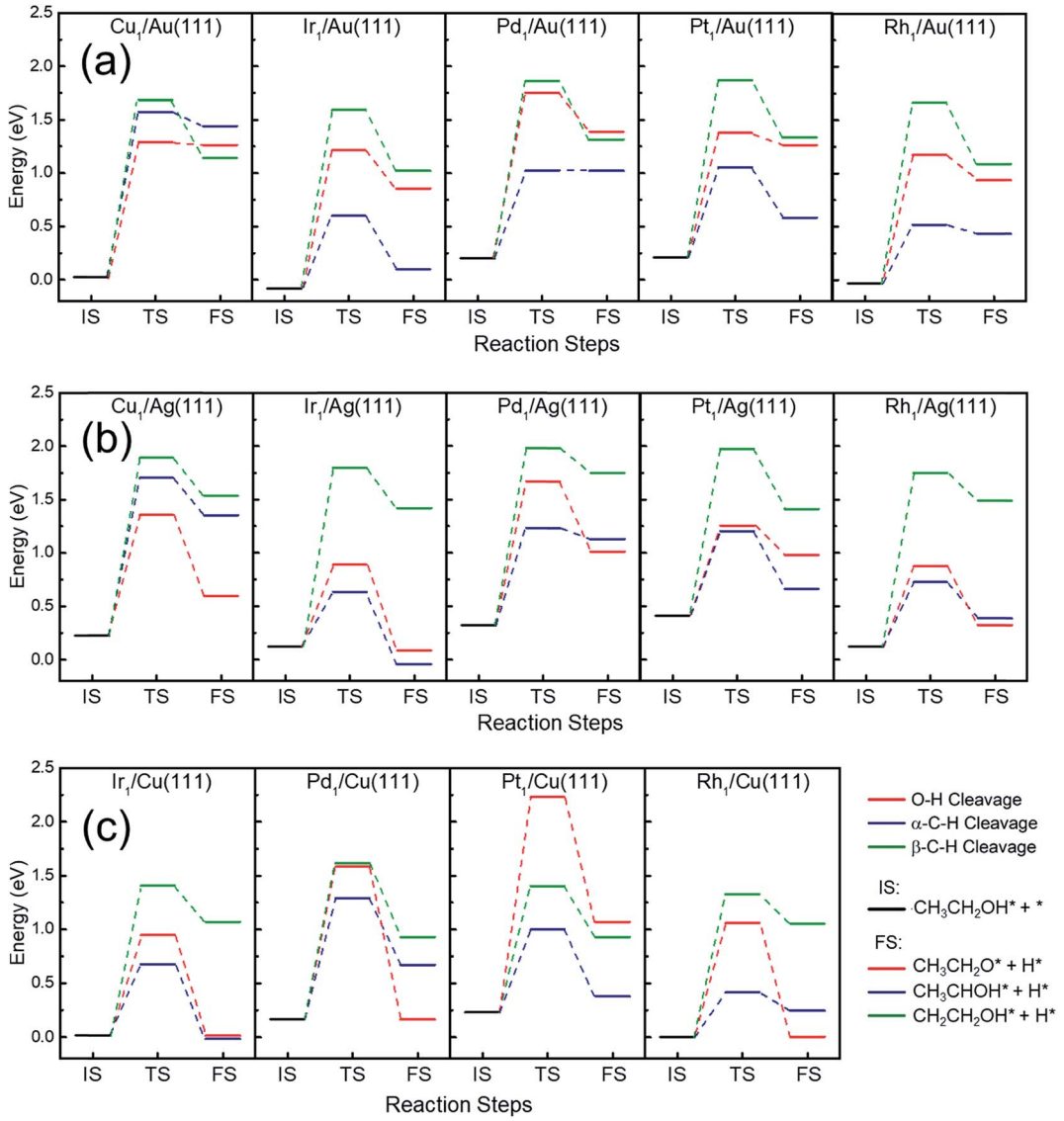

Fig. 4 Free energy profiles of the three possible initial dehydrogenation reactions of ethanol at $X_1/Y(111)$ (X = Cu, Ir, Pd, Pt, and Rh; Y = Au (a), Ag (b), and Cu (c)) surfaces. IS, TS, and FS indicate the initial, transition, and final states, respectively.

studies;[27,41] no significant changes were found in the optimized geometries, binding energies, or energy barriers. The entropic correction to EtOH adsorption was applied with a temperature of 298 K.

2.2 Modeling methods

Each Au, Ag, and Cu(111) substrate was modeled as a three-layer slab with a (3×3) unit cell. A vacuum layer of at least 12 Å was used to separate periodic images of the slab. In the calculations, the bottom layer of the slab was fixed to bulk, while the two topmost layers were allowed to relax. Convergence tests for a five-layer model were used to compare with the three-layer model; no significant difference was found (Table S1†). Adsorption of EtOH was tested in a (4×4) unit cell with a Pd_1/Au(111) model; the adsorption energy was found to vary by no more than 5% and no significant change was found in the adsorption configuration. With the previous conclusion that the reactivity of EtOH dehydrogenation mainly depends on the binding energy and the adsorption geometry,[26,27] we expect that a (4×4) unit cell should lead to a highly similar conclusion compared with a (3×3) unit cell. The single-atom alloy surface was constructed by substituting one surface atom with a doping element (Scheme 1). The single-atom alloy surfaces are denoted as X_1/Y(111), where X = {Cu, Ir, Pd, Pt, and Rh} and Y = {Au, Ag, and Cu}. The lattice constant for each slab was calculated using Vegard's law,[64] according to the bimetallic composition. The surface segregation energies E_{Seg} (of both bare and H-bound surfaces) were calculated by swapping one substrate element from the sublayer with the doped single-atom element,[65,66]

$$E_{Seg} = E_{Swapped} - E_{Original} \quad (1)$$

where $E_{Original}$ and $E_{Swapped}$ are respectively the energies of the surface before and after swapping.

3. Results and discussion

3.1 Surface stability of the single-atom alloys

Before evaluating the reactivity of the single-atom catalysts, their surface stability was estimated by calculating their segregation energies, using eqn (1), both with a clean surface and with H-bound to the dopant (Fig. 1). The single-atom alloy surfaces in quadrant I have positive segregation energies with and without an adsorbed H atom, indicating that they are thermodynamically stable. For the surfaces in quadrant II, while their segregation energies are negative on the clean surface, they are stable with adsorbed H due to a favorable interaction between the dopant and H. Since some other possible adsorbates, as intermediates of EtOH activation (*e.g.*, O), bind stronger than H,[44] they are expected to provide a stronger driving force to stabilize the surface.[67,68] Therefore, it is expected that surfaces in quadrant II are thermodynamically stable under the reaction conditions for EtOH activation.

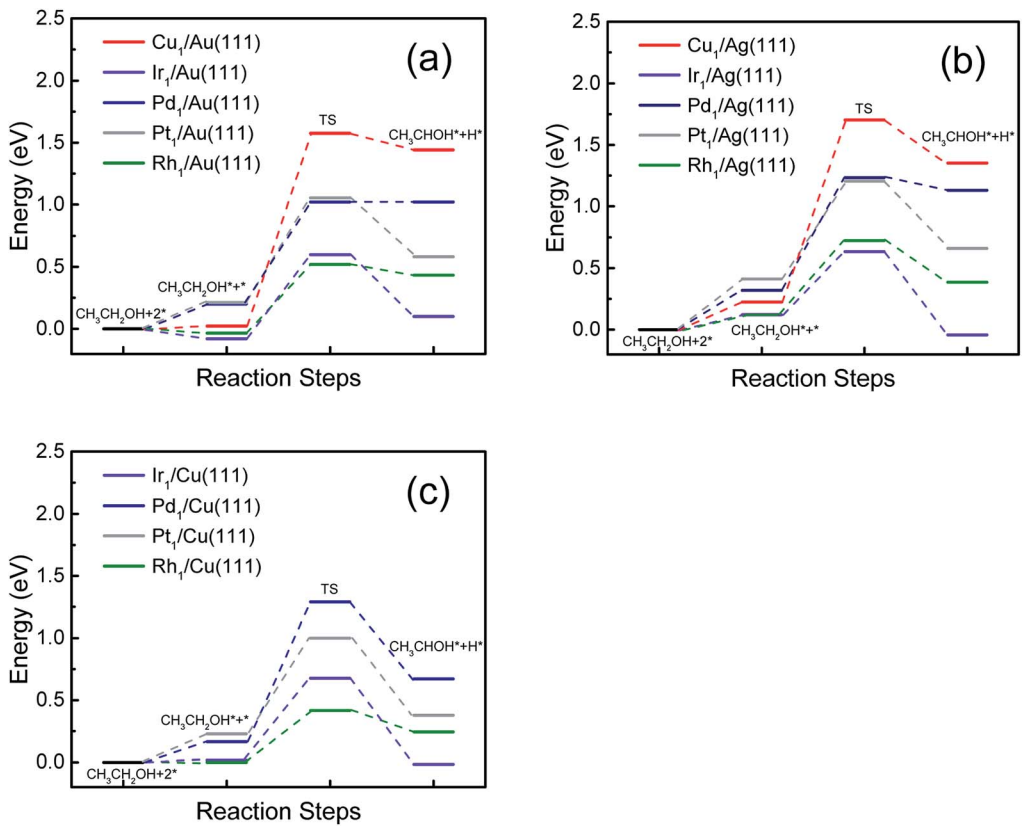

Fig. 5 Free energy profiles of the α-C–H dehydrogenation selectivity of ethanol on single-atom doped catalysts alloyed into (a) Au(111), (b) Ag(111), and (c) Cu(111).

Finally, quadrant III indicates that the two $Cu_1/Y(111)$ surfaces are not stable neither under vacuum nor H-bound conditions. In general, it can be seen that $X_1/Au(111)$ and $X_1/Cu(111)$ are stable, while $X_1/Ag(111)$ tends to be stable only with a H adsorbate. In addition, we calculated the reaction energies associated with the dopants leaching out from the (111) surface (Table S2 and Fig. S1a†). These thermodynamic results show that leaching is highly endothermic and therefore unfavorable. The calculated segregation energies of the two surface isolated dopants show that the single-atom alloys have these segregation energies close to zero, with the exceptions of $Ir_1/Au(111)$ (−0.25 eV) and $Ir_1/Ag(111)$ (−0.38 eV) (see Table S3 and Fig. S1b†). It is expected that with suitable experimental control of dispersed surface dopants, segregation will be reduced due to the long distance between dopants. These results are in good agreement with recent experimental studies showing that a single-atom alloy surface can be stable after synthesis and catalysis.[48,69] Given that most of these surfaces are thermodynamically stable under catalytic conditions, and advanced kinetically controlled synthesis methods are also available to prepare meta-stable surfaces,[39,40,70,71] we consider all of these surfaces for the calculations of EtOH activation in this study.

3.2 Hydrogen and carbon on the surface

Two of the unique features of alloying strong- and weak-binding elements are the tunable hydrogen and carbon bindings to the surface. These properties can directly influence the dehydrogenation reaction by providing facile hydrogen desorption and resistance to carbon-coking.[41] Here, we evaluate the hydrogen desorption energies and carbon binding energies at the single-atom alloy surfaces alloyed with strong- and weak-binding elements (Fig. 2 and 3).

As we can see from the hydrogen desorption profiles, the Pd, Pt, and Rh single-atom alloys show a decrease in the energy of the rate-determining step for hydrogen desorption (Fig. 2). Interestingly, compared to Rh(111), the rate-determining step at the $Rh_1/Y(111)$ surface changes from the association of hydrogen to the desorption of a hydrogen molecule (Fig. 2d). On the other hand, the $Ir_1/Y(111)$ surfaces have significantly higher energy barriers as compared to Ir(111). This is because H_2 cannot be stabilized at the Ir atop site, leading to hindered recombination of hydrogen at the Ir atop site (Fig. 2e).[26] Therefore, it is expected that on $Ir_1/Y(111)$, hydrogen desorbs at the Au/Ag/Cu surfaces due to facile H diffusion.[56] Most of the single-atom alloy surfaces studied here lead to easier hydrogen

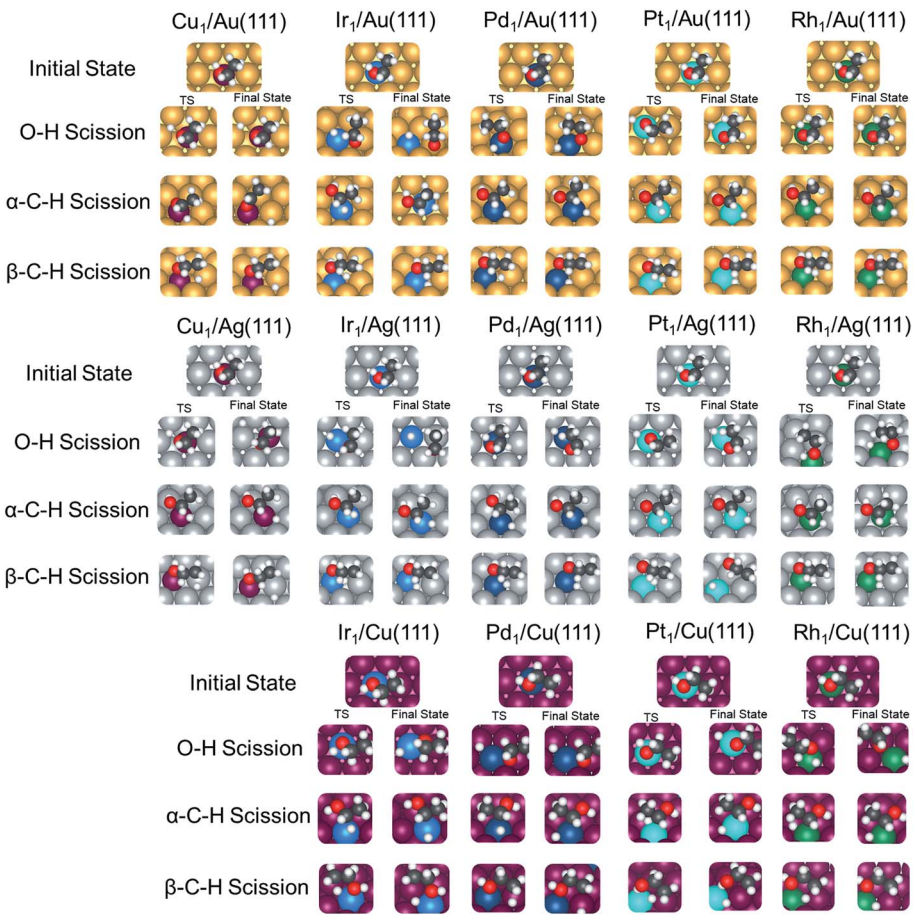

Fig. 6 Initial, transition, and final states of EtOH dehydrogenation on $X_1/Y(111)$ (X = Cu, Ir, Pd, Pt, and Rh; Y = Au, Ag, and Cu) surfaces. Gold, purple, sliver, blue, deep blue, teal, green, red, grey, and white spheres represent Au, Cu, Ag, Ir, Pd, Pt, Rh, O, C, and H, respectively.

desorption, which provides more sites for ethanol activation and easier hydrogen production at relatively low temperatures.

To evaluate the carbon-coking effect on a surface during ethanol reforming, a previous combined theoretical and experimental study has shown that carbon-coking can be qualitatively correlated with trends in the carbon binding energy on the alloy surfaces.[41] Therefore, here we evaluated the carbon binding energies of each alloyed triatomic ensemble of the single-atom alloy surface (Fig. 3). As expected, all the single-atom alloy surfaces considered have significantly weakened carbon binding energies, which suggests that they are more resistant to carbon coking as compared to Ir, Pd, Pt, and Rh(111). To draw a more generalized conclusion, a nearly linear correlation between carbon binding energy and the d-band centers (average energy of the surface d-electrons) of the triatomic ensembles is shown in Fig. 3b. This clearly indicates that alloying weak-binding elements into Ir/Pd/Pt/Rh leads to a down-shift of the surface d-band, which in turn weakens binding energies on these alloyed ensembles and gives them coke-resisting properties.

3.3 Ethanol dehydrogenation at single-atom alloys

The initial dehydrogenation selectivities of EtOH at single-atom alloys were calculated with the ClNEB method, as shown in Fig. 4; (tabulated results are in Table S4†). With the exception of two single-Cu alloys, Cu_1/Au(111) and Cu_1/Ag(111), the α-C–H activation barriers are lower than those of β-C–H and O–H. For Cu_1/Au(111) and Cu_1/Ag(111), O–H activation is favored because Cu is an oxophilic element.[72,73] However, due to the high reaction barriers (>1.0 eV) at the Cu_1 sites, these two surfaces are not expected to facilitate EtOH activation except at elevated temperature.[74] Interestingly, with the exception of Pt_1/Cu(111), the α-C–H selective surfaces have activation energies in the order of: β-C–H > O–H > α-C–H. This is in excellent agreement with our design principle that a single-atom element alloyed into a weak-binding substrate could inhibit β-C–H scission since there is no active site near the $–CH_3$ group (Scheme 1).

Fig. 5 shows a comparison of α-C–H activation barriers at different surfaces. It can be seen that Ir_1 and Rh_1 single-atom sites generally have lower adsorption free energies of EtOH as well as lower α-C–H activation barriers as compared to the other surfaces, indicating that Ir_1/Y(111) and Rh_1/Y(111) are promising catalysts for EtOH activation. Together with the experimental and theoretical results that Ir-alloys are generally less tunable for H-binding while Rh-alloys are highly tunable,[39,40,44,70,71,75] we expect that the single-Rh atom alloys in this study are the best candidates for applications with EtOH activation due to their facile hydrogen evolution kinetics as shown in Fig. 2.

Fig. 6 shows the geometries of the initial, transition, and final states of EtOH initial dehydrogenation. It can be seen that

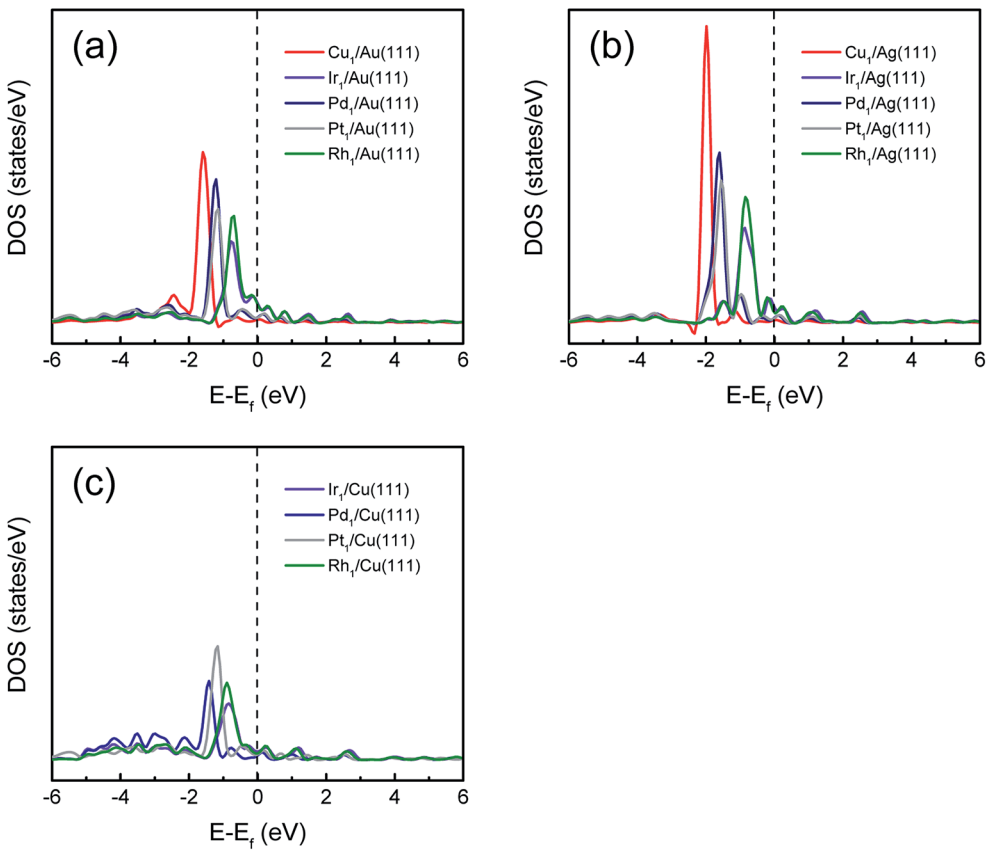

Fig. 7 Calculated projected density of states (PDOS) of d-electrons of the single-atom element doped on (a) Au(111), (b) Ag(111), and (c) Cu(111) surfaces. The black dashed lines represent the Fermi energy level (E_f).

the favorable EtOH adsorption geometries are similar, with the O–H group pointing to the dopant and the C–C bond nearly parallel to the surface.[26] Except for the single-Ir surfaces, the dissociated H atoms in the final states are adsorbed at the 3-fold hollow site of the X_1Y_2 triatomic ensemble as described in Scheme 1. In terms of the single-Ir surfaces, H prefers to stay near the Ir-atop site, consistent with our recent study that H tends to migrate to the Ir-atop site from a 3-fold hollow site.[40] Though all reaction states are similar with EtOH partial oxidation at monometallic surfaces,[26,27,76,77] it is clear that the β-carbon binds to the weak-binding substrate instead of the doped single-atom element on our surfaces (Fig. 6). Taken together with results of previous studies showing that stronger adsorbate binding energies would lead to lower dehydrogenation barriers,[27] this explains why β-C–H scission is not favorable: the driving forces from the Au/Ag/Cu sites are too weak to cleave a β-C–H. We expect that this geometric design principle of single-atom surface alloys could be extended to the selective dehydrogenation of other H-rich organics including hydrocarbons and other alcohols.

3.4 Reactivity analysis

To understand the trends of the dehydrogenation barriers, the projected density of states (PDOS) of d-electrons of the single-atom element doped at the substrate surfaces were calculated, as shown in Fig. 7. Though the widths of the d-bands are similar across the elements, it can be seen that the narrowest bands for Ir and Rh are closer to the Fermi level (black dashed line), than those of Pd, Pt, and Cu. The d-band of Cu is furthest from the Fermi level, indicative of weak adsorbate bindings and low activity for EtOH activation.[78] Interestingly, the magnitude of the d-bands is highly dependent on the substrate, in the order of Ag(111) > Au(111) > Cu(111), indicating differences in charge transfer from the doped single-atom element to these noble metal surfaces. A detailed correlation between charge transfer and the activation barriers can be found in Fig. S2.† In general, these PDOS qualitatively explain the EtOH activation reactivity of O–H and α-C–H activations at different surfaces, where Ir and Rh, Pd and Pt, and Cu are respectively active, moderate, and inert for dehydrogenation. This is similar to their monometallic surfaces.[78] Since β-C–H activation occurs primarily on the noble metal, our PDOS results cannot be correlated with its activation energies. We will discuss the trends of β-C–H activation later in this paper.

To analyze the trends of the activation energies, a generalized Brønsted–Evans–Polanyi (BEP) relationship was developed as shown in Fig. 8a. It can be seen that though the overall trends are nearly linear, the β-C–H activation energies are

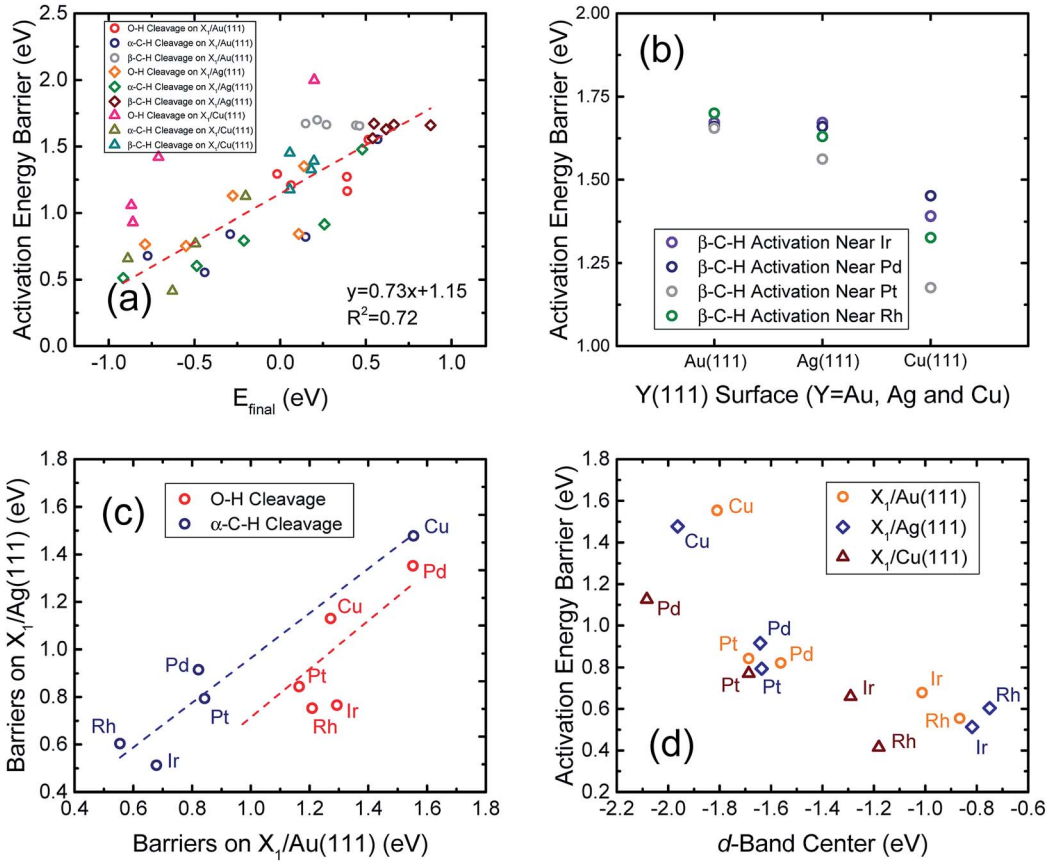

Fig. 8 (a) BEP correlation between the activation energy barrier and the final state. E_{final} is relative to the bare slab and ethanol (in the gas phase). (b) β-C–H activation energy *vs.* the three (111) substrates. (c) Correlation of the O–H and α-C–H activation barriers between X_1/Au(111) and X_1/Ag(111) (X = Cu, Ir, Pd, Pt, and Rh). (d) Correlation between the d-band center of the single-atom element and the α-C–H activation barrier.

similar among the same type of substrates (grey circle, deep red diamond, and teal triangle points, in Fig. 8a) indicating that the single-atom dopant does not significantly influence the reaction activity of β-C–H scission, which occurs at an inert site. Fig. 8b shows that as compared to X_1/Ag(111) and X_1/Cu(111), β-C–H scission barriers on X_1/Au(111) are highly uniform. Also, Pt_1/Y(111) tends to have the lowest β-C–H activation barriers, compared with other single-atom dopants. Compared to Au and Ag(111), β-C–H is relatively more tunable on Cu(111). This is because the strain effect becomes relatively more significant than the electronic effect after alloying since Cu has a smaller lattice constant than Au and Ag. Fig. 8c compares the activation barriers of O–H and α-C–H at the same single-atom element on Au(111) and Ag(111). We can see that although the regression slopes are close to unity, the intercept of α-C–H scission is close to the origin while that of O–H scission is negative, indicating that α-C–H scission is fairly independent of the substrate, while the electronic effect from Ag (as seen in Fig. 7) lowers the O–H scission barrier. Since the reaction kinetics on X_1/Cu(111) deviate from the overall BEP trends (Fig. 8a), we do not compare the Cu surfaces with those of Au and Ag. Finally, since α-C–H barriers correlate best with the generalized BEP relationship (Fig. 8a), we plot the correlation between the activation barrier and the calculated d-band center of the doped single-atom element (Fig. 8d). It can be clearly seen that, as the primary selectivity at the single-atom alloy surfaces in this study, the energy barriers can be qualitatively described by a linear relationship with the calculated d-band center of the alloying element. This indicates that the reactivity of EtOH dehydrogenation at other similar single-atom alloys can be directly screened and predicted using the d-band center as the descriptor, since we know the most likely selectivity for EtOH dehydrogenation on such a type of single-atom alloy.

4. Conclusions

In this paper, we have shown that single-atom alloy catalysts are promising for selective EtOH partial oxidation. We found that strong-binding single-atom elements (Ir, Pd, Pt, and Rh) doped onto weak-binding inert close-packed surfaces (Au, Ag, and Cu) will lead to highly active and selective initial dehydrogenation at α-C–H. Not only being thermodynamically stable, these catalysts also feature facile hydrogen evolution and resistance to carbon coking. We expect that this catalytic design strategy for alcohol dehydrogenation has practical significance, especially for tailoring selective alcohol oxidation to higher value products. We show that with a theoretical knowledge of alloying effects, a rational design of the geometry of an alloy ensemble can help to target the selectivity of a complicated reaction.

Conflicts of interest

There are no conflicts to declare.

Acknowledgements

Financial support was provided by the National Science Foundation (CHE-1764230 and CHE-1807847) and the Robert A. Welch Foundation (F-1841). Calculations were done at the National Energy Research Scientific Computing Center and the Texas Advanced Computing Center. H. L. acknowledges the 2017 Hamilton/Schoch Fellowship and 2018 Department Excellence Fellowship.

References

1 Y. Lin and S. Tanaka, *Appl. Microbiol. Biotechnol.*, 2006, **69**, 627–642.
2 Y. Sun and J. Cheng, *Bioresour. Technol.*, 2002, 1–11.
3 S. P. S. Badwal, S. Giddey, A. Kulkarni, J. Goel and S. Basu, *Appl. Energy*, 2015, 80–103.
4 P. D. Vaidya and A. E. Rodrigues, *Chem. Eng. J.*, 2006, **117**, 39–49.
5 F. Frusteri and S. Freni, *J. Power Sources*, 2007, **173**, 200–209.
6 S. Nanda, R. Rana, Y. Zheng, J. A. Kozinski and A. K. Dalai, *Sustainable Energy Fuels*, 2017, **1**, 1232–1245.
7 B. Xu, R. J. Madix and C. M. Friend, *J. Am. Chem. Soc.*, 2010, **132**, 16571–16580.
8 D. Zanchet, J. B. O. Santos, S. Damyanova, J. M. R. Gallo and J. M. C. Bueno, *ACS Catal.*, 2015, **5**, 3841–3863.
9 C. Lamy, S. Rousseau, E. M. Belgsir, C. Coutanceau and J. M. Léger, *Electrochim. Acta*, 2004, 3901–3908.
10 J. Rass-Hansen, H. Falsig, B. Jørgensen and C. H. Christensen, *J. Chem. Technol. Biotechnol.*, 2007, **82**, 329–333.
11 Z. F. Xu and Y. Wang, *J. Phys. Chem. C*, 2011, **115**, 20565–20571.
12 Z. Xu and Y. Wang, *ACS Symp. Ser.*, 2013, **1133**, 135–151.
13 L. X. Dai, X. Y. Wang, S. S. Yang, T. Zhang, P. J. Ren, J. Y. Ye, B. Nan, X. D. Wen, Z. Y. Zhou, R. Si, C. H. Yan and Y. W. Zhang, *J. Mater. Chem. A*, 2018, **6**, 11270–11280.
14 R. Rizo, R. M. Arán-Ais, E. Padgett, D. A. Muller, M. J. Lázaro, J. Solla-Gullón, J. M. Feliu, E. Pastor and H. D. Abruña, *J. Am. Chem. Soc.*, 2018, **140**, 3791–3797.
15 E. J. Evans, H. Li, S. Han, G. Henkelman and C. B. Mullins, *ACS Catal.*, 2019, **9**, 4516–4525.
16 E. D. Wang, J. B. Xu and T. S. Zhao, *J. Phys. Chem. C*, 2010, **114**, 10489–10497.
17 J. Gong and C. B. Mullins, *J. Am. Chem. Soc.*, 2008, **130**, 16458–16459.
18 B. N. Zope, D. D. Hibbitts, M. Neurock and R. J. Davis, *Science*, 2010, **330**, 74–78.
19 R. M. Williams, S. H. Pang and J. W. Medlin, *Surf. Sci.*, 2014, **619**, 114–118.
20 M. Zhu, G. Sun and Q. Xin, *Electrochim. Acta*, 2009, **54**, 1511–1518.
21 D. D. Hibbitts and M. Neurock, *J. Catal.*, 2013, **299**, 261–271.
22 D. C. Papageorgopoulos, Q. Ge and D. A. King, *J. Phys. Chem.*, 1995, **99**, 17645–17649.
23 S. M. Gates, J. N. Russell and J. T. Yates, *Surf. Sci.*, 1985, **159**, 233–255.

24 J. L. Davis and M. A. Barteau, *Surf. Sci.*, 1987, **187**, 387–406.
25 S. M. Gates, J. N. Russell and J. T. Yates, *Surf. Sci.*, 1986, **171**, 111–134.
26 E. J. Evans, H. Li, W. Y. Yu, G. M. Mullen, G. Henkelman and C. B. Mullins, *Phys. Chem. Chem. Phys.*, 2017, **19**, 30578–30589.
27 H. Li and G. Henkelman, *J. Phys. Chem. C*, 2017, **121**, 27504–27510.
28 S. E. Davis, M. S. Ide and R. J. Davis, *Green Chem.*, 2013, 17–45.
29 M. B. Griffin, A. A. Rodriguez, M. M. Montemore, J. R. Monnier, C. T. Williams and J. W. Medlin, *J. Catal.*, 2013, **307**, 111–120.
30 T. Mallat and A. Baiker, *Chem. Rev.*, 2004, **104**, 3037–3058.
31 C. Keresszegi, T. Mallat, J. D. Grunwaldt and A. Baiker, *J. Catal.*, 2004, **225**, 138–146.
32 Q. S. Meng, Y. L. Shen, J. Xu and J. L. Gong, *Chin. J. Catal.*, 2012, **33**, 407–415.
33 X. Liu, B. Xu, J. Haubrich, R. J. Madix and C. M. Friend, *J. Am. Chem. Soc.*, 2009, **131**, 5757–5759.
34 B. Xu, X. Liu, J. Haubrich and C. M. Friend, *Nat. Chem.*, 2010, **131**, 5757–5759.
35 J. J. Spivey and A. Egbebi, *Chem. Soc. Rev.*, 2007, **36**, 1514.
36 J. L. C. Fajín, M. N. D. S. Cordeiro, F. Illas and J. R. B. Gomes, *J. Catal.*, 2014, **313**, 24–33.
37 B. A. Sexton, K. D. Rendulic and A. E. Huges, *Surf. Sci.*, 1982, **121**, 181–198.
38 P. Kunal, H. Li, B. L. Dewing, L. Zhang, K. Jarvis, G. Henkelman and S. M. Humphrey, *ACS Catal.*, 2016, **6**, 4882–4893.
39 G. W. Piburn, H. Li, P. Kunal, G. Henkelman and S. M. Humphrey, *ChemCatChem*, 2018, **10**, 329–333.
40 H. Guo, H. Li, K. Jarvis, H. Wan, P. Kunal, S. G. Dunning, Y. Liu, G. Henkelman and S. M. Humphrey, *ACS Catal.*, 2018, **8**, 11386–11397.
41 H. Li, E. J. Evans, C. B. Mullins and G. Henkelman, *J. Phys. Chem. C*, 2018, **122**, 22024–22032.
42 P. Liu and J. K. Nørskov, *Phys. Chem. Chem. Phys.*, 2001, **3**, 3814–3818.
43 W. Tang and G. Henkelman, *J. Chem. Phys.*, 2009, **130**, 194504.
44 H. Li, K. Shin and G. Henkelman, *J. Chem. Phys.*, 2018, **149**, 174705.
45 L. G. Verga, A. E. Russell and C. K. Skylaris, *Phys. Chem. Chem. Phys.*, 2018, **20**, 25918–25930.
46 W. Y. Yu, G. M. Mullen, D. W. Flaherty and C. B. Mullins, *J. Am. Chem. Soc.*, 2014, **136**, 11070–11078.
47 P. Tereshchuk and J. L. F. Da Silva, *J. Phys. Chem. C*, 2012, **116**, 24695–24705.
48 G. Giannakakis, M. Flytzani-Stephanopoulos and E. C. H. Sykes, *Acc. Chem. Res.*, 2018, **52**, 237–247.
49 G. Kyriakou, M. B. Boucher, A. D. Jewell, E. A. Lewis, T. J. Lawton, A. E. Baber, H. L. Tierney, M. Flytzani-Stephanopoulos and E. C. H. Sykes, *Science*, 2012, **335**, 1209–1212.
50 Z. T. Wang, R. A. Hoyt, M. El-Soda, R. J. Madix, E. Kaxiras and E. C. H. Sykes, *Top. Catal.*, 2018, **61**, 328–335.
51 F. R. Lucci, L. Zhang, T. Thuening, M. B. Uhlman, A. C. Schilling, G. Henkelman and E. Charles, *Surf. Sci.*, 2018, **677**, 296–300.
52 M. T. Darby, R. Réocreux, E. C. H. Sykes, A. Michaelides and M. Stamatakis, *ACS Catal.*, 2018, **8**, 5038–5050.
53 T. Yamada, T. Kojima, E. Abe, S. Kameoka, Y. Murakami, P. Gille and A. P. Tsai, *J. Am. Chem. Soc.*, 2018, **140**, 3838–3841.
54 Y. Zhuang, J. P. Chou, P. Y. Liu, T. Y. Chen, J. Jung Kai, A. Hu and H. Y. Tiffany Chen, *J. Mater. Chem. A*, 2018, **6**, 23326–23335.
55 Z. W. Chen, L. X. Chen, C. C. Yang and Q. Jiang, *J. Mater. Chem. A*, 2019, 3492–3515.
56 M. Pan, D. W. Flaherty and C. B. Mullins, *J. Phys. Chem. Lett.*, 2011, **2**, 1363–1367.
57 J. L. Davis and M. A. Barteau, *Surf. Sci.*, 1988, **197**, 123–152.
58 J. P. Perdew, K. Burke and M. Ernzerhof, *Phys. Rev. Lett.*, 1996, **77**, 3865–3868.
59 P. E. Blöchl, *Phys. Rev. B: Condens. Matter Mater. Phys.*, 1994, **50**, 17953–17979.
60 W. Kohn and L. J. Sham, *Phys. Rev.*, 1965, **140**, A1133.
61 S. Grimme, J. Antony, S. Ehrlich and H. Krieg, *J. Chem. Phys.*, 2010, **132**, 154104.
62 H. Monkhorst and J. Pack, *Phys. Rev. B: Solid State*, 1976, **13**, 5188–5192.
63 G. Henkelman, B. P. Uberuaga and H. Jónsson, *J. Chem. Phys.*, 2000, **113**, 9901–9904.
64 A. R. Denton and N. W. Ashcroft, *Phys. Rev. A*, 1991, **43**, 3161–3164.
65 L. Zhang and G. Henkelman, *J. Phys. Chem. C*, 2012, **116**, 20860–20865.
66 L. Zhang, R. Iyyamperumal, D. F. Yancey, R. M. Crooks and G. Henkelman, *ACS Nano*, 2013, **7**, 9168–9172.
67 H. Y. Kim and G. Henkelman, *ACS Catal.*, 2013, **3**, 2541–2546.
68 H. An, H. Ha, M. Yoo and H. Y. Kim, *Nanoscale*, 2017, **9**, 12077–12086.
69 M. T. Darby, M. Stamatakis, A. Michaelides and E. C. H. Sykes, *J. Phys. Chem. Lett.*, 2018, 5636–5646.
70 H. Li, L. Luo, P. Kunal, C. S. Bonifacio, Z. Duan, J. C. Yang, S. M. Humphrey, R. M. Crooks and G. Henkelman, *J. Phys. Chem. C*, 2018, **122**, 2712–2716.
71 S. García, L. Zhang, G. W. Piburn, G. Henkelman and S. M. Humphrey, *ACS Nano*, 2014, **8**, 11512–11521.
72 Y. Liu, H. Li, W. Cen, J. Li, Z. Wang and G. Henkelman, *Phys. Chem. Chem. Phys.*, 2018, **20**, 7508–7513.
73 L. Zhang, H. Y. Kim and G. Henkelman, *J. Phys. Chem. Lett.*, 2013, **4**, 2943–2947.
74 P. Ferrin, D. Simonetti, S. Kandoi, E. Kunkes, J. A. Dumesic, J. K. Nørskov and M. Mavrikakis, *J. Am. Chem. Soc.*, 2009, **131**, 5809–5815.
75 J. V. Pande, A. B. Bindwal, Y. B. Pakade and R. B. Biniwale, *Int. J. Hydrogen Energy*, 2018, **43**, 7411–7423.
76 Y. Choi and P. Liu, *Catal. Today*, 2011, **165**, 64–70.
77 J. H. Wang, C. S. Lee and M. C. Lin, *J. Phys. Chem. C*, 2009, **113**, 6681–6688.
78 J. Zhang, X. M. Cao, P. Hu, Z. Zhong, A. Borgna and P. Wu, *J. Phys. Chem. C*, 2011, **115**, 22429–22437.